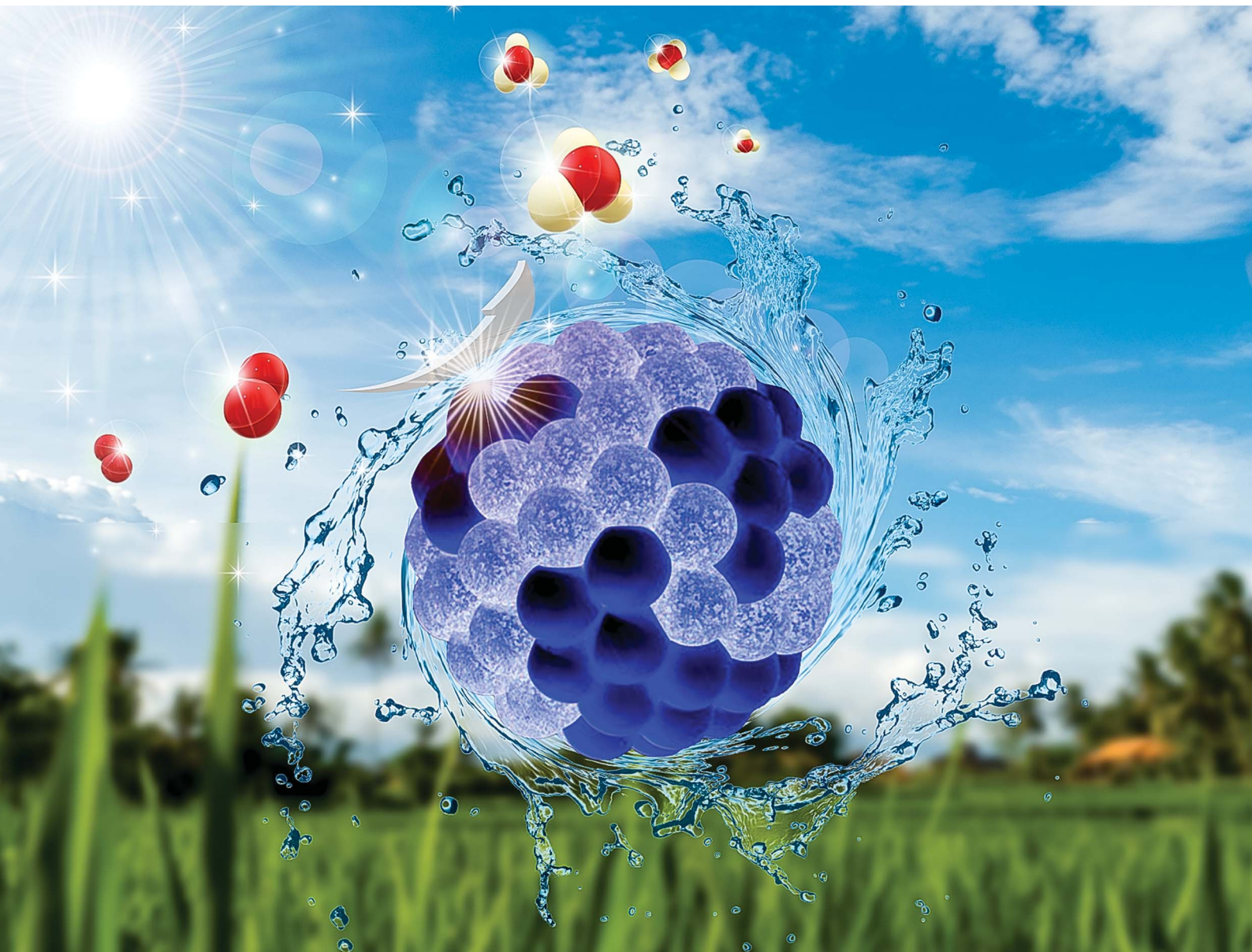


Chemical Science

rsc.li/chemical-science



ISSN 2041-6539

EDGE ARTICLE

Hyoyoung Lee *et al.*
Phase-selective active sites on ordered/disordered titanium
dioxide enable exceptional photocatalytic ammonia
synthesis



Cite this: *Chem. Sci.*, 2021, **12**, 9619

All publication charges for this article have been paid for by the Royal Society of Chemistry

Phase-selective active sites on ordered/disordered titanium dioxide enable exceptional photocatalytic ammonia synthesis†

Jinsun Lee,^{‡,ab} Xinghui Liu,^{‡,ab} Ashwani Kumar,^{‡,ab} Yosep Hwang,^{ab} Eunji Lee,^c Jianmin Yu,^{ab} Young Dok Kim^b and Hyoyoung Lee  ^{*abde}

Photocatalytic N_2 fixation to NH_3 via defect creation on TiO_2 to activate ultra-stable $\text{N}\equiv\text{N}$ has drawn enormous scientific attention, but poor selectivity and low yield rate are the major bottlenecks. Additionally, whether N_2 preferentially adsorbs on phase-selective defect sites on TiO_2 in correlation with appropriate band alignment has yet to be explored. Herein, theoretical predictions reveal that the defect sites on disordered anatase (A_d) preferentially exhibit higher N_2 adsorption ability with a reduced energy barrier for a potential-determining-step (* N_2 to NNH^*) than the disordered rutile (R_d) phase of TiO_2 . Motivated by theoretical simulations, we synthesize a phase-selective disordered-anatase/ordered-rutile TiO_2 photocatalyst ($\text{Na-A}_d/\text{R}_d$) by sodium-amine treatment of P25- TiO_2 under ambient conditions, which exhibits an efficient NH_3 formation rate of $432 \mu\text{mol g}^{-1} \text{h}^{-1}$, which is superior to that of any other defect-rich disordered TiO_2 under solar illumination with a high apparent quantum efficiency of 13.6% at 340 nm. The multi-synergistic effects including selective N_2 chemisorption on the defect sites of Na-A_d with enhanced visible-light absorption, suitable band alignment, and rapid interfacial charge separation with R_d enable substantially enhanced N_2 fixation.

Received 14th June 2021
Accepted 29th June 2021

DOI: 10.1039/d1sc03223b
rsc.li/chemical-science

1. Introduction

Ammonia (NH_3) is not only the most important industrial chemical but also the most promising carbon-free energy alternative due to its high hydrogen density (17.8 wt%).¹ Industrial NH_3 production has heavily relied on the traditional Haber–Bosch process (150–350 atm, 350–550 °C), which consumes ~2% of the global energy supply and accounts for 1.6% of total global CO_2 emissions.^{2,3} To circumvent these issues, an alternative N_2 fixation method operating under milder reaction conditions is necessary, and in response to this, electrocatalytic and photocatalytic N_2 reduction reactions (NRRs) have emerged as promising choices as they can be performed under green and sustainable conditions.^{4–9}

However, the reduction of N_2 to NH_3 under ambient conditions is extremely difficult due to the inherent nature of the $\text{N}\equiv\text{N}$ (bond dissociation energy: 940.95 kJ mol^{–1}) along with additional thermodynamically challenging multistep processes. Although recent progress in the photocatalytic NRR demonstrated that N_2 fixation can be promoted using various semiconductors including two-dimensional materials such as Mxenes,¹⁰ TiO_2 nanosheets,¹¹ Au/end- CeO_2 ,¹² $\text{Bi}_5\text{O}_7\text{X}$ (X = Cl, Br, I) nanotubes,^{13,14} and single atoms anchored on various supports,^{15,16} the selectivity and NH_3 yield rate for most of them are far from satisfactory. The two main reasons for the poor photocatalytic NRR are (i) poor interfacial charge transfer (CT) due to the high recombination rate of photo-generated holes and electrons and (ii) weak N_2 adsorption ability.⁹ Therefore, a novel strategy to design photocatalysts with efficient charge separation and high N_2 adsorption ability is urgently needed to improve the performance of the photocatalytic NRR.

More recently, defect engineering of photocatalysts has received immense attention as it offers unsaturated sites for N_2 chemisorption, further weakening the $\text{N}\equiv\text{N}$ and lowering the activation energy barrier for the NRR.¹⁷ For instance, Hirakawa *et al.* reported that introducing oxygen vacancies (O_v) on commercial JRC-TIO-6 (rutile phase, R) can boost the photocatalytic NRR with a solar-to-chemical conversion (SCC) efficiency of 0.02%.¹⁸ Zhao *et al.* elucidated that O_v along with lattice strain rich ultrathin anatase (A) nanosheets obtained via a facile copper-doping strategy exhibited strong chemisorption and activation of N_2 and water, resulting in high rates of NH_3

^aCenter for Integrated Nanostructure Physics (CINAP), Institute for Basic Science (IBS), 2066 Seoburo, Jangan-gu, Suwon 16419, Republic of Korea. E-mail: hyoyoung@skku.edu

^bDepartment of Chemistry, Sungkyunkwan University, 2066 Seoburo, Jangan-gu, Suwon 16419, Republic of Korea

^cDepartment of Energy Science, Sungkyunkwan University, 2066 Seoburo, Jangan-gu, Suwon 16419, Republic of Korea

^dDepartment of Biophysics, Sungkyunkwan University, 2066 Seoburo, Jangan-gu, Suwon 16419, Republic of Korea

^eCreative Research Institute, Sungkyunkwan University, 2066 Seoburo, Jangan-gu, Suwon 16419, Republic of Korea

† Electronic supplementary information (ESI) available. See DOI: [10.1039/d1sc03223b](https://doi.org/10.1039/d1sc03223b)

‡ These authors contributed equally.



evolution under visible-light irradiation.¹¹ However, the defect sites introduced additionally act as the recombination centers of the photogenerated carriers and limit the efficiency of the reported photocatalysts. Therefore, despite such significant efforts on the defect engineering of the TiO_2 surface, the lack of fundamental understanding of the nature of phase-selective defect sites, high recombination rate, poor visible-light harvesting ability, harsh defect-engineering procedure, and insufficient chemisorption/activation of $\text{N}\equiv\text{N}$ severely hamper the photocatalytic NRR kinetics. In addition, one important issue remained unanswered “Whether N_2 chemisorption happens at all the O_v sites, or it is specific to a particular phase of $\text{P25-}\text{TiO}_2$ (A: 75% and R: 25%) in correlation with appropriate band alignment for activating N_2 and subsequent conversion to NH_3 ” deserves to be further investigated.

Herein, we first investigated the N_2 fixation activity of single-phase ordered (R_o , A_o) and disordered (R_d , A_d) TiO_2 by theoretical calculations, which suggested that creating O_v on the anatase phase of TiO_2 (A_d) is conducive for N_2 adsorption, significantly reducing the energy barrier of the potential-determining step (PDS: $^*\text{N}_2$ to NNH^*), boosting the intrinsic NRR over the rutile phase (R_d). Encouraged by theoretical predictions, we developed a facile strategy to synthesize a phase-selective A_d/R_o heterostructure by alkali metal (Na) amine treatment of P25- TiO_2 (Na-A_d/R_o) under ambient conditions, which exhibits an efficient adsorption/desorption kinetics of N_2/NH_3 specifically on the Na-A_d phase and faster hole transport through the heterointerface region of the R_o phase hindering charge recombination, significantly facilitating water oxidation to produce necessary protons for efficient N_2 fixation. The novel Na-A_d/R_o without any co-catalyst possesses a superior NH_3 formation rate ($432 \mu\text{mol g}^{-1} \text{h}^{-1}$), which is ~ 125 and 5.5 times

higher than that of bare TiO_2 and Na-A_d, respectively under solar illumination, exhibiting one of the superior NRR performances with a high selectivity of 97.6%. Theoretical simulations clearly revealed that high intrinsic N_2 chemisorption ability with the reduced energy barrier for PDS selectively originated from defect sites on Na-A_d rather than R_o and Li-R_d (Li-EDA treated R_o) along with a suitable band alignment promoting the NRR over hydrogen (H_2) generation on Na-A_d/R_o. The multi-synergistic effects induced by phase-selective defect sites on Na-A_d/R_o, increased visible light absorption, and enhanced interfacial charge separation are found to be the key factors for higher photocatalytic activity.

2. Results and discussion

2.1 Theoretical calculation predictions

To understand the nature of phase-selective defect sites, density functional theory (DFT) calculations were first conducted to study the intrinsic N_2 adsorption ability on the specific phase of ordered (R_o, A_o) and defect-rich disordered (Li-R_d, Na-A_d) TiO_2 samples. The optimized atomic models with adsorbed N_2 molecules on Li-R_d, Na-A_d, R_o, and A_o are presented in Fig. 1a-d. The computed N_2 adsorption energy (E_{ads}) values on R_o and A_o are close to 0 eV, indicating that the adsorption/activation of N_2 in the absence of defect-sites on A_o and R_o hardly takes place at room temperature (Fig. 1e). In contrast, N_2 can readily adsorb on Na-A_d with an E_{ads} of -0.21 eV (thermodynamically favorable), while N_2 adsorption on Li-R_d is an endothermic process ($E_{\text{ads}}: +0.61$ eV), suggesting that the defect sites on the A_d phase of TiO_2 selectively prefer N_2 chemisorption over the R_d phase. Furthermore, we examined the Gibbs free energy diagrams of the NRR along the alternating pathway on Na-A_d and Li-R_d

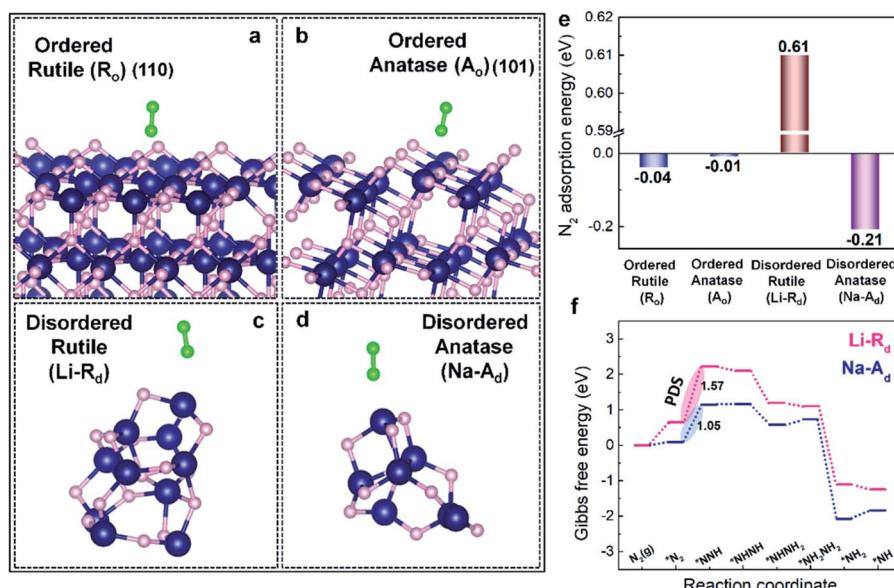


Fig. 1 DFT calculations of N_2 adsorption on ordered/disordered TiO_2 and the reaction pathway. (a-d) Optimized atomic models with N_2 molecules on R_o , A_o , Li-R_d , and Na-A_d . (e) N_2 adsorption energy on R_o , A_o , Li-R_d , and Na-A_d atomic models. (f) Gibbs free energy (ΔG) profiles of N_2 fixation over Li-R_d and Na-A_d along the alternating pathway. Navy, pink, light green balls represent titanium, oxygen, and nitrogen, respectively.



(Fig. 1f). Similar to the E_{ads} trend, the first hydrogenation step (PDS: *N_2 to NNH^*) on Na-A_d is energetically more favorable than that on Li-R_d , boosting NH_3 synthesis for the former. In a nutshell, DFT calculations certify that phase-selective defect sites on the A_d phase of TiO_2 (Na-A_d) show higher N_2 adsorption ability with superior intrinsic NRR activity over defect sites on the R_d phases of TiO_2 (Li-R_d).

2.2 Synthesis and structural analysis of ordered/disordered TiO_2 photocatalysts

Motivated by the theoretical predictions, a series of selectively ordered/disordered phases of P25- TiO_2 were synthesized by

alkali-metal amine treatment also known as “dissolving-metal reduction” following our previous reports with slight modifications,^{19,20} as it is an effective strategy to create O_v on the specific phase of TiO_2 . Using lithium and the sodium ethylenediamine complex (Li, Na-EDA) with different reduction abilities of the solvated electrons can selectively create defect sites (Ti^{3+} adjacent to O_v) on R_o and A_o phases, respectively, to generate Li-R_d and Na-A_d , under mild conditions. The X-ray diffraction (XRD) (Fig. S1†) peaks indicate a gradual decrease in the specific phase of P25- TiO_2 with the reaction time (1, 3, and 7 days) by Li/Na-EDA treatments. Fig. 2a reveals that either the R_o or A_o phase in mixed-phase P25- TiO_2 nearly disappeared

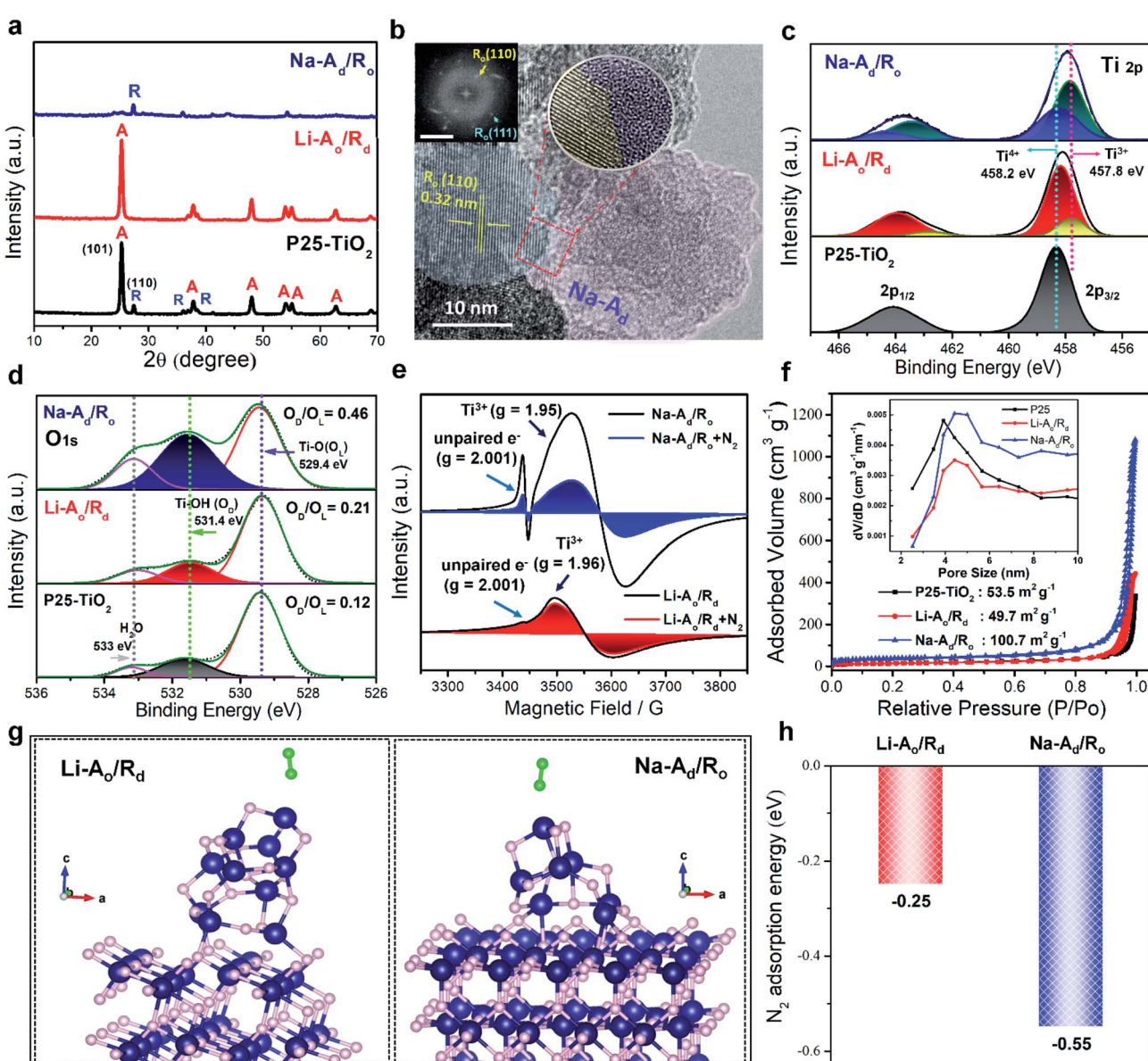


Fig. 2 Structural characterization and simulation for N_2 adsorption on P25- TiO_2 , $\text{Li-A}_o/\text{R}_d$, and $\text{Na-A}_d/\text{R}_o$. (a) The powder X-ray diffraction spectra (XRD). (b) HR-TEM image of $\text{Na-A}_d/\text{R}_o$ (inset scale bar: 5 nm^{-1}). XPS spectra of (c) Ti 2p and (d) O 1s. (e) Electron paramagnetic resonance (EPR) spectra of $\text{Li-A}_o/\text{R}_d$ and $\text{Na-A}_d/\text{R}_o$ before and after N_2 saturation at 77 K. (f) N_2 adsorption–desorption isotherms of P25- TiO_2 , $\text{Li-A}_o/\text{R}_d$ and $\text{Na-A}_d/\text{R}_o$ (inset, corresponding pore-size distribution). (g) Optimized atomic models with N_2 molecules on $\text{Li-A}_o/\text{R}_d$ and $\text{Na-A}_d/\text{R}_o$. (h) N_2 adsorption energy of $\text{Li-A}_o/\text{R}_d$ and $\text{Na-A}_d/\text{R}_o$. Navy, pink, light green balls represent titanium, oxygen, and nitrogen, respectively.

after 7 days of treatment, denoted as Li-A_o/R_d and Na-A_d/R_o, respectively, which is additionally supported by Raman spectra (Fig. S2†). The high-resolution transmission electron microscopy (HRTEM) image with the selected area electron diffraction (SAED) pattern of Na-A_d/R_o revealed the formation of a distinct heterointerface between the crystalline phase of R_o and disordered phase of Na-A_d along with uniform distribution of Ti and O as confirmed by EDX mapping (Fig. 2b and S3†). The ordered lattice fringes with a spacing of 3.6 Å and 2.1 Å can be assigned to the A_o(101) and R_o(111) plane (Fig. S4a and b†), respectively, along with each disordered phase starting from the surface to the core after 5 days of treatment, further confirming the random distribution of atoms in the disordered phase by HADDF-STEM (Fig. S4c–f†). Thus, our phase-selective disordered method successfully introduces defect sites on the specific phase of the TiO₂ surface, which could selectively capture inert N₂ and boost the NRR.

To investigate the chemical composition and valence states of the elements over the selectively reduced TiO₂ catalysts, high-resolution X-ray photoelectron spectroscopy (XPS) was employed. Compared to P25-TiO₂, the binding energy (BE) of the Ti 2p doublet peaks at 458.2 and 463.9 eV consistent with the typical characteristic peaks of Ti 2p_{1/2} and Ti 2p_{3/2} for Ti⁴⁺ showed a negative shift to lower BE for Li-A_o/R_d and Na-A_d/R_o, attributed to the appearance of a low-valence Ti³⁺ at 457.8 and 462.8 eV on the surface (Fig. 2c).²¹ The removal of lattice oxygen left excessive electrons trapped by the adjacent Ti⁴⁺ species, generating Ti³⁺ sites or unpaired electrons, which could behave as an active center for surface adsorption of key N₂ adsorbates. The O 1s XPS spectra exhibit three peaks at 529.4, 531.4, and 533 eV, attributed to the TiO₂ lattice oxygen (Ti–O, O_L), surface hydroxyl group (Ti–OH, defective oxygen: O_D) originating from the reaction between chemisorbed water and the oxygen vacancy of disordered TiO₂, and adsorbed H₂O molecule, respectively (Fig. 2d). In Fig. S5a–d,† there is a gradual increase of Ti³⁺ sites with a simultaneous increase of O_D/O_L ratio for Li-A_o/R_d (0.21) and Na-A_d/R_o (0.46) as a function of reaction time, confirming the generation of Ti³⁺ with oxygen vacancies during alkali-metal amine treatment.²² Furthermore, the absence of all possible impurities like EDA (ethylenediamine), alkali ions (Na⁺), and chloride (Cl[−]) in the samples which may cause exaggerated and erroneous NH₃ yield was confirmed by N 1s, Na 1s, and Cl 2p XPS spectra, respectively, (Fig. S5e–h†).²³ We further quantified the amount of Ti³⁺ on Li-A_o/R_d, Na-A_d/R_o, Li-R_d, and Na-A_d by XPS peak deconvolution and CO₂ temperature-programmed desorption (CO₂-TPD) measurements, as summarized in Table 1. Atomic percentages of Ti³⁺/Ti⁴⁺ over the samples in the Ti 2p orbitals of XPS were calculated (Fig. S6†). CO₂-TPD was also investigated to monitor surface defects (Ti³⁺) existing in disordered structures (Fig. S7 and Table S1†). CO₂-TPD analysis between 150 and 500 °C resulted in two ranges: one range between 170 and 204 °C attributed to CO₂ molecules bound to a regular five-coordinate Ti⁴⁺ site in the ordered TiO₂ and the other over 280 °C corresponds to CO₂ molecules bound to defective Ti³⁺ species in the disordered structure, indicating Ti³⁺ species bonded CO₂ more strongly than the regular five-coordinate Ti⁴⁺ sites.²⁴ From the above results, it was found

that the surface defects (Ti³⁺) with oxygen vacancies on phase-selective disordered TiO₂ were successfully created by Li/Na-EDA treatment while P25-TiO₂ had a few defect sites.

The N₂ adsorption capacity is one of the key factors impacting NH₃ synthesis. The N₂ physisorption ability of defect sites on Na-A_d/R_o and Li-A_o/R_d compared to P25-TiO₂ was firstly investigated by electron paramagnetic resonance (EPR) analysis. Each catalyst (20 mg) was separately placed in a quartz EPR tube and analyzed at 77 K before and after N₂ (99.999%) gas saturation (20 torr) (Fig. 2e). Commercial TiO₂ with Ti⁴⁺ sites are diamagnetic (3d⁰, S = 0) in nature whereas defective TiO₂ contains paramagnetic Ti³⁺ centers (3d¹, S = 1/2) also known as “spin-active defects” generated due to oxygen vacancies.²⁵ Both Na-A_d/R_o and Li-A_o/R_d show distinctive EPR signals of paramagnetic Ti³⁺ (g = 1.96) and unpaired electrons (g = 2.001) trapped in the oxygen vacancies while P25-TiO₂ showed a negligible EPR signal (Fig. S8†). The Na-A_d/R_o exhibits a much higher number and signature of spin active Ti³⁺ sites compared to Li-A_o/R_d, suggesting a high density of electron spin polarization arising from the spin active Ti³⁺ centers on Na-A_d/R_o. Especially, these spin active Ti³⁺ centers containing unpaired electrons in Na-A_d can effectively interact with the N₂ adsorbates expected to be effective for N₂ fixation, which is corroborated by the significantly quenched EPR signal of Na-A_d/R_o after N₂ saturation (Fig. 2e). Additionally, the BET specific surface area of all samples was examined by N₂ adsorption–desorption measurements in Fig. 2f, which revealed that the P25-TiO₂, Li-A_o/R_d, and Na-A_d/R_o are mesoporous in nature with an average pore distribution in the range of 3.5 to 4.5 nm. The specific surface area for Na-A_d/R_o (100.67 m² g^{−1}) is much higher than that of Li-A_o/R_d (49.7 m² g^{−1}) with a slightly larger average pore size compared to P25-TiO₂, implying higher N₂ adsorption with better mass transport, suitable for enhancing N₂ fixation. Interestingly, the Na-A_d (143.74 m² g^{−1}) exhibited a much higher surface area than Li-R_d (14.508 m² g^{−1}) even with abundant Ti³⁺ species in both cases, indicating high intrinsic N₂ adsorption ability of the defect sites on Na-A_d, consistent with the calculated N₂ adsorption energy (Fig. 1e and S9†). To further understand the chemisorption ability of surface defects on Na/Li-TiO₂ samples compared to P25-TiO₂, N₂/NH₃-TPD measurements were then employed (Fig. S10 and Table S2†).^{26,27} The area of N₂ desorption follows the order of Na-A_d > Na-A_d/R_o > Li-A_o/R_d ~ Li-R_d > P25-TiO₂, indicating that Na-A_d and Na-A_d/R_o have higher and stronger N₂ adsorption capacities than Li-R_d and Li-A_o/R_d. Meanwhile, NH₃-TPD was evaluated to monitor the NH₃ desorption from the catalysts.²⁷ Most of the NH₃ desorbed on Na-A_d/R_o and Na-A_d relatively at a low temperature (100–194 °C), which indicates its weak adsorption on defect sites compared to Li-A_o/R_d and Li-R_d, implying much faster reaction kinetics and mass diffusion for the former. Likewise, the optimized N₂-E_{ad} of Na-A_d on Na-A_d/R_o (−0.55 eV) exhibits more negative values than that of Li-R_d on Li-A_o/R_d (−0.25 eV) as calculated by DFT (Fig. 2g and h) and AIMD simulations (Movies S1–S6†),^{28–32} suggesting that N₂ adsorption is favorable on the defect sites of Na-A_d over Li-R_d in the heterostructure, further verifying our above-mentioned claims. Note that we also considered the N₂-E_{ad} at the interface between Na-A_d and R_o,



Table 1 Summary of photoactivity and selectivity of various phase-selective ordered/disordered TiO_2 samples for photocatalytic N_2 fixation

Sample	Surface area ^a ($\text{m}^2 \text{ g}^{-1}$)	E_g^b (eV)	Quantity of Ti^{3+} ^c (%/mmol g^{-1})	k_{H_2} ^d ($\mu\text{mol g}^{-1} \text{ h}^{-1}$)	k_{NH_3} ^e ($\mu\text{mol g}^{-1} \text{ h}^{-1}$)	Selectivity of N_2 reduction ^f (%)	Selectivity of H_2 evolution ^g (%)	NH_3 yield per BET ^h ($\mu\text{mol h}^{-1} \text{ m}^{-2} \text{ g}$)
P25- TiO_2	53.5	3.12	2.6/0.1	18.3	3.4	21.8	78.2	3.2
Li-A _d / R_d	49.7	2.84	21.8/0.4	213	23	14.0	86.0	23.1
Na-A _d / R_o	100.7	2.65	62.1/0.6	15.7	432	97.6	2.4	214.5
Na-A _d	143.7	2.66	73.4/NA	Trace	77.1	NA	NA	26.8
Li-R _d	14.5	2.75	74.8/NA	Trace	4.2	NA	NA	14.5

^a Determined by Brunauer–Emmett–Teller (BET) for N_2 adsorption/desorption isotherms. ^b Determined by a plot of the Kubelka–Munk function versus the energy of light absorbed. ^c Quantification of Ti^{3+} concentration over all samples measured by XPS (%) and CO_2 -TPD (mmol g^{-1}).

^d The H_2 production rate (k_{H_2}) during the N_2 reduction reaction under solar light under closed conditions. All the H_2 gas was detected by syringe using GC-TCD. ^e The NH_3 production rate (k_{NH_3}) during the N_2 reduction reaction under solar light determined by cation exchange chromatography (IC). ^f Selectivity for N_2 reduction (%) = $3k_{\text{NH}_3}/R_e \times 100\%$. Electron consumption rate for the reduced products ($\mu\text{mol g}^{-1} \text{ h}^{-1}$), $R_e = 2k_{\text{H}_2} + 3k_{\text{NH}_3}$. ^g Selectivity for H_2 evolution (%) = $2k_{\text{H}_2}/R_e \times 100\%$. ^h NH_3 yield per BET surface area = $k_{\text{NH}_3} \times 50 \text{ mg/BET}$.

showing that N_2 hardly adsorbs during the relaxation process (Fig. S11†). These results concluded that N_2 molecules selectively adsorb on the surface defects of the Na-A_d phase, neither on the Li-R_d phase nor at the heterointerface.

2.3 Photocatalytic N_2 reduction activity and durability over ordered/disordered TiO_2 samples

To confirm the effect of phase-selective defect sites on N_2 fixation, we assessed the efficacy of Na-A_d/R_o and other catalysts for

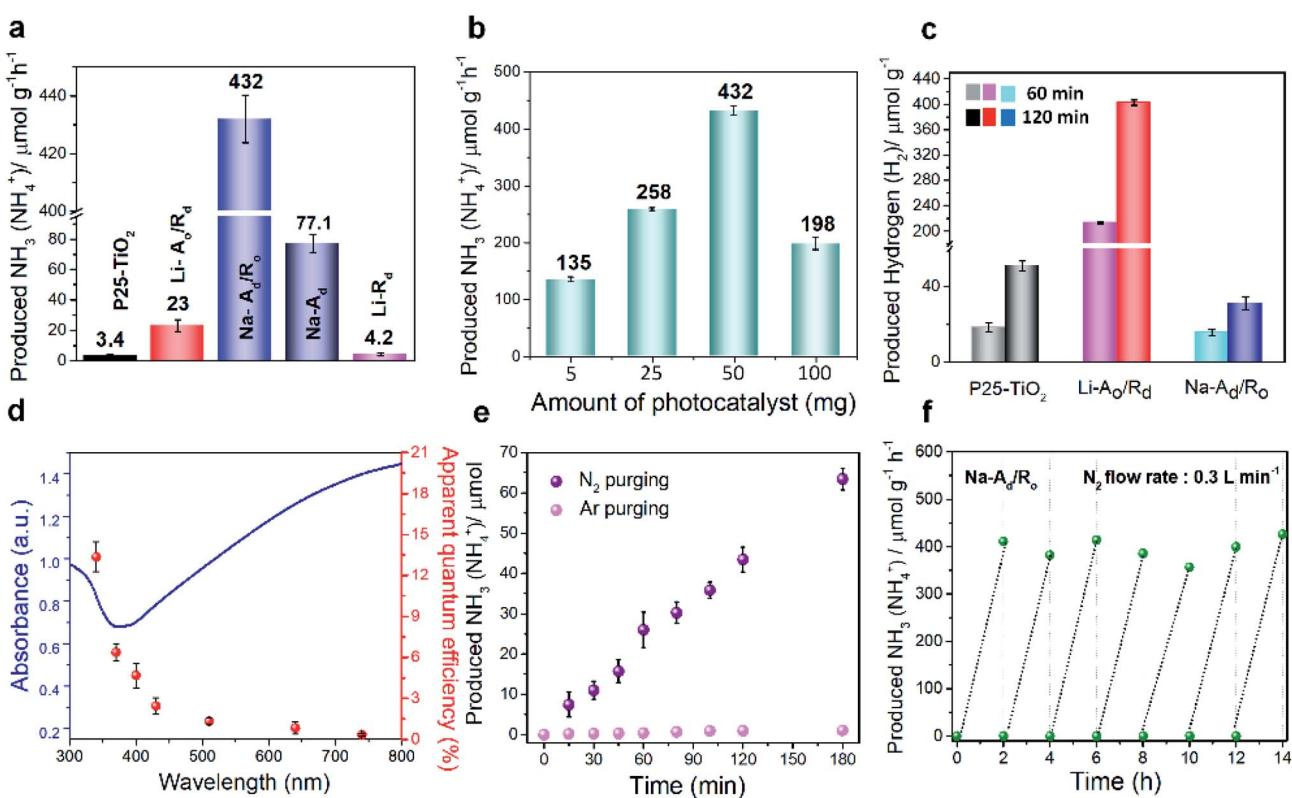


Fig. 3 Photocatalytic N_2 fixation activities of various ordered/disordered TiO_2 samples. (a) The rate of produced NH_3 (NH_4^+) over P25- TiO_2 , Li-A_d/ R_d , Na-A_d/ R_o , Li-R_d and Na-A_d/ R_o in N_2 saturated water with IPA (14%) as the hole/hydroxyl radical scavenger under solar illumination. (b) The rate of produced NH_3 (NH_4^+) for Na-A_d/ R_o at various amounts of the catalyst for photocatalytic N_2 reduction. (c) The rate of produced H_2 over P25- TiO_2 , Li-A_d/ R_d and Na-A_d/ R_o in N_2 saturated water with IPA (14%) as the hole scavenger under solar illumination. (d) UV-vis diffuse reflectance spectrum (UV-DRS, left axis) and calculated apparent quantum efficiency (AQE, right axis) for N_2 fixation over Na-A_d/ R_o under monochromatic light irradiation. (e) Time-dependent rates of produced NH_3 (NH_4^+) for Na-A_d/ R_o under N_2 and Ar gas purging. (f) Cycling test of photocatalytic N_2 fixation over Na-A_d/ R_o .



the photocatalytic NRR, as schematically illustrated in Fig. S12†. Generally, the catalyst needs to be well-dispersed in a mixture containing 50 mL of N₂-saturated water and 7 mL of isopropyl alcohol (IPA) as the hole and hydroxyl radical scavenger under 1 sun illumination with continuous N₂ gas flow (99.999%, flow rate: 0.3 L min⁻¹, cc). One can see that the 7 day treated Na-A_d/R_o exhibits the highest rate of NH₄⁺ production (432 μmol g⁻¹ h⁻¹) with a high NRR selectivity of 97.6%, followed by Na-A_d (77.1 μmol g⁻¹ h⁻¹), Li-A_o/R_d (23 μmol g⁻¹ h⁻¹), Li-R_d (4.2 μmol g⁻¹ h⁻¹) and P25-TiO₂ (3.4 μmol g⁻¹ h⁻¹), benefitted by excellent N₂ adsorption ability of the Na-A_d phase, as measured by ion chromatography (IC) (Fig. 3a and Table S3†). The Na-A_d/R_o showed the highest NH₃ yield at an optimum amount of 50 mg, while the NH₃ yield rate gradually decreased at a higher amount due to the poor penetration of photons and hindered mass diffusion (Fig. 3b).³³ It is interesting to note that in the absence of IPA, Na-A_d/R_o also showed a reasonable NH₃ production rate of 327 μmol g⁻¹ h⁻¹ along with oxygen (O₂) generation as confirmed by GC-TCD (Fig. S13a and b†), with a stoichiometric ratio of NH₃ to O₂ (2 : 1.5), N₂ + 3H₂O → 2NH₃ + 3/2O₂, suggesting that the photogenerated holes are efficiently consumed *via* the water oxidation process. The NH₃ yield rate and apparent quantum efficiency (AQE) for Na-A_d/R_o can be comparable and superior to most of the reported photocatalysts with/without hole scavengers under solar light irradiation (Table S4†). Additionally, photocatalytic nitrate (NO₃⁻) reduction activity was evaluated; since N=O bonds have relatively lower dissociation energy (204 kJ mol⁻¹) than N≡N bonds (945 kJ mol⁻¹),³⁴ Na-A_d/R_o exhibits the highest NO₃⁻ reduction activity under sunlight and 100 W LED light compared to Li-A_o/R_d and P25-TiO₂, confirming the superior intrinsic activity for the former (Fig. S13c†). Furthermore, high NRR activity for Na-A_d/R_o over other catalysts was supported by the indophenol-blue method as an alternative analytical method, which can be used to ensure the produced NH₄⁺, as our solution is neutral or slightly basic before and the after reaction, as detected with a pH meter (Fig. S14a-c†).³⁵ To evaluate the effect of different ratios of Na-A_d and R_o phases on the NRR performance, we synthesized two different ratios of Na-A_d/R_o (90 : 10 and 50 : 50) and compared their NRR performance with main Na-A_d/R_o (75 : 25) (Fig. S14d†). As revealed in Fig. S14d,† Na-A_d/R_o (75 : 25) exhibited the highest NH₃ yield compared to other control ratios (90 : 10 and 50 : 50). Additionally, we conducted a blank experiment in the absence of any catalysts under the same conditions, which resulted in a non-traceable amount of NH₃ as confirmed by IC and the indophenol blue method, revealing that the photocatalytic NRR is the sole reason for a high rate of NH₃ production rather than any possible contamination from air or other impurities (Fig. S14d†). For the control experiment, we synthesized a heterostructure containing 75% of Li-R_d and 25% of A_o and performed the NRR under the same conditions. However, its NH₃ yield (4.8 μmol g⁻¹ h⁻¹) quantified by IC was negligible because of poor N₂ adsorption ability on the abundant Li-R_d phase. The superior intrinsic N₂ adsorption ability of Na-A_d over Li-R_d was further corroborated by the BET specific surface area-normalized NH₃ yield (Table 1), which strongly

reinforces the significance of phase-selective active sites for N₂ fixation.

To confirm the origin of the NH₃ generated from the supplied N₂ gas, ¹⁵N₂ (98 atom%, ¹⁵N) isotope labeling experiments were carefully performed for 50 min at 8 sccm controlled by the mass flow control (MFC) system (Fig. S15†). Double coupling of ¹⁵NH₄⁺ and triple coupling of ¹⁴NH₄⁺ are identified by ¹H nuclear magnetic resonance (¹H NMR), signifying that the N₂ gas is the only source of NH₃, further supported by mass spectra,¹⁸ EDS analysis of Na-A_d/R_o and additional control NRR experiments under Ar-saturated solution (Fig. S15c and S16†).^{23,36} Importantly, some reported papers claimed that oxygen vacancies introduced on catalysts could behave as active sites for water dissociation and boost HER activity.^{22,37-39} Hence, it is necessary to examine the HER activity and selectivity over disordered catalysts in a closed system under the same conditions for the NRR (Fig. 3c and Table 1). Interestingly, the Na-A_d/R_o (H₂ yield rate: 15.7 μmol g⁻¹ h⁻¹) exhibits poor HER activity compared to Li-A_o/R_d (H₂ yield rate: 213 μmol g⁻¹ h⁻¹), which may be attributed to the high surface coverage of N₂ molecules on the defect sites of Na-A_d rather than the proton (H⁺), but an opposite trend to O_V defective sites on Li-R_d, as revealed by experimental analysis and theoretical calculations. Additionally, hydrazine (N₂H₄) and nitrate acid (HNO₃) are possible by-products that can be detected by the Watt and Chrisps method and IC, respectively, and negligible N₂H₄ and a trace amount of NO₃⁻ (0.17 μmol g⁻¹ h⁻¹) were detected during the NRR, suggesting high selectivity of NH₃ synthesis for Na-A_d/R_o (Fig. S17, S18 and Table S5†).⁴⁰ To confirm the effect of trace NO₃⁻ produced during the reaction on the total yield of NH₃ for Na-A_d/R_o, twice the amount of trace NO₃⁻ (0.34 μmol g⁻¹ h⁻¹) was added into the catalyst dispersed solution and examined under solar light for 2 h under the same NRR conditions. The NH₃ yield of only 0.357 ppm (1.05 μmol h⁻¹ g⁻¹) detected by IC was well within the error range. Therefore, the influence of trace NO₃⁻ on the total yield of NH₃ was negligible. In Fig. 3d, the wavelength-dependent quantum efficiency (QE) experiment for N₂ fixation on Na-A_d/R_o under monochromatic light irradiation closely fits the absorption spectrum, showing approximately 13.6%, 6.4%, 4.7%, 2.4%, 1.3%, 0.8% and 0.3% at 340, 370, 400, 430, 510, 640 and 740 nm, respectively. However, the apparent QE of Na-A_d/R_o over 500 nm is inconsistent with the visible light absorption distribution in the ultraviolet-visible spectrum. Creating oxygen defects on disordered TiO₂ can harvest visible light, however, the excited electrons which are located at deep trap states are unable to be utilized for the NRR because they cannot be excited and migrated thermally to the CB as well as their states are located well below the N₂/NH₃ redox potential, which makes them inactive for N₂ fixation.⁴¹ Although these trap sites are inactive for N₂ fixation, they are the main sites for enhancing the N₂ adsorption on the surface of the Na-A_d accelerating NRR process.

Besides superior activity, the durability of the catalyst is another crucial parameter for practical applications. The cycling tests for Na-A_d/R_o were conducted for 3 h under 1 sun illumination with continuous N₂ gas supply showing linearly produced NH₄⁺, quantified by IC (Fig. 3e) and the indophenol-



blue method (Fig. S19†). Moreover, the rate of NH_3 yield for $\text{Na-A}_d/\text{R}_o$ remained constant for 7 consecutive cycles (Fig. 3f), suggesting its excellent stability towards the NRR. After stability tests, careful examination of XPS, XRD, and TEM characterization on $\text{Na-A}_d/\text{R}_o$ phases shows no distinct changes over surface Ti^{3+} and the amorphous structure of the Na-A_d junction with the crystalline R_o phase, indicating the robustness of $\text{Na-A}_d/\text{R}_o$ towards the photocatalytic NRR, however, a slight decrease of the O_v sites was observed probably due to water molecules or reactants/intermediates after stability tests (Fig. S20†). From the results, we found that the photocatalytic NRR showed a close relationship with a specific type of phase-selective absorption site for N_2 fixation rather than all possible surface defects sites. Although sufficient defect sites on Li-R_d and $\text{Li-A}_o/\text{R}_d$ were present, poor intrinsic N_2 adsorption ability and favorable HER kinetics significantly hamper the formation of NH_3 and its selectivity (Table 1).¹⁶

2.4 Optical and charge transfer (CT) properties and band alignment over ordered/disordered TiO_2 samples

To develop an in-depth mechanistic understanding of the outstanding NRR performance of $\text{Na-A}_d/\text{R}_o$ over the other catalysts, the electronic band position was determined based on the Tauc plots, UPS, and valence-band XPS spectra (VB-XPS) (Fig. 4a–e and S21†).⁴² It is known that a heterointerface between two different phases is an important factor leading to rapid interfacial CT and modulation of the energy band alignment.¹⁹ The secondary-electron cut-off energy for Na-A_d and R_o was measured by UPS as 16.40 and 16.3 eV, respectively (Fig. 4a), and the Fermi level (E_f) was then estimated to be –0.04 and 0.06 eV (vs. NHE, pH = 7), respectively. The VB positions with respect to E_f were determined by VB-XPS as 2.10 and 1.86 eV, respectively (Fig. 4b). To further obtain the conduction-band position (E_{CB}) of Na-A_d and R_o , the energy bandgap (E_g) was also obtained by linear extrapolation of the Tauc plots ($\alpha h\nu$)^{1/2} vs. $h\nu$, obtaining indirect bandgap energies of 2.49 and 3.04 eV, respectively (Fig. 4c). Consequently, the E_{CB} of Na-A_d and R_o can be further determined as –0.39 and –1.18 eV, respectively (vs. NHE, pH = 7) (Fig. 4d). In general, the energy band at the interface of two different semiconductors would be rearranged by a band alignment through contacts until E_f is aligned at the same level. The possible electronic band structure of $\text{Na-A}_d/\text{R}_o$ (Fig. 4d) is finally depicted after rearrangement. For Na-A_d , both CB and VB potentials are downshifted while those for R_o are upshifted, which is a type-II band structure, indicating that the CB potential of Na-A_d (–0.39 eV) is suitable for N_2/NH_3 and the VB potential of R_o (1.81 eV) is much closer for the water oxidation reaction.⁴³ Combined with a suitable band-alignment and enhanced visible-light absorption, possible interfacial charge separation at the heterointerface where electrons on Na-A_d are consumed to activate the adsorbed N_2 molecules and holes on R_o oxidize the water molecules in the meantime (Fig. 4d) corroborates the superior NRR selectivity of $\text{Na-A}_d/\text{R}_o$. Additionally, we also delineated the possible electronic band structure of $\text{Li-A}_o/\text{R}_d$ and P25-TiO_2 (Fig. S21†). Interestingly, we found that the CB potential of $\text{Li-A}_o/\text{R}_d$ and P25-TiO_2 is placed

nearby HER potentials with low N_2 adsorption, resulting in poor NRR selectivity (14%) and high HER kinetics (86%) for $\text{Li-A}_o/\text{R}_d$.

In order to further understand the interfacial charge carrier dynamics, photoluminescence (PL) spectra of P25-TiO_2 , Na-A_d , and $\text{Na-A}_d/\text{R}_o$ were examined (Fig. 4e). All catalysts exhibit a distinct PL peak centered approximately at 506 nm upon excitation by a 375 nm laser. After defect formation, the PL intensity of Na-A_d is quenched at 550 nm corresponding to defect states attributed to Ti^{3+} on oxygen vacancies and further quenched for $\text{Na-A}_d/\text{R}_o$. This PL quenching behavior corresponds to facile CT between Na-A_d and R_o at the interface. We then used TRPL spectroscopy to probe charge carrier dynamics over Na-A_d and $\text{Na-A}_d/\text{R}_o$ films by electrophoretic deposition (10 V, 15 s each on the ITO substrate, inset) in Fig. 4f. The light intensity decay curves through two relaxation pathways can be fitted with an exponential equation as shown below:⁴⁴

$$f(t) = A_0 + A_1(\exp(-t/\tau_1)) + A_2(\exp(-t/\tau_2)), \quad (1)$$

where A_0 is a constant for the baseline offset, τ_1 is fast decay time responsible for exciton recombination with the involvement of surface states or electron transfer, and τ_2 is slow decay time correlated with the indirect recombination of self-trapped excitons with trapped electrons. A_1 and A_2 are the corresponding decay amplitudes. The obtained parameters of the TRPL data are listed in Table S6.† For both Na-A_d and $\text{Na-A}_d/\text{R}_o$, the increased amplitude of short-lived excited species (A_1) and decreased amplitude of long-lived excited species (A_2) as compared to P25-TiO_2 are observed, especially the A_2 for $\text{Na-A}_d/\text{R}_o$ dramatically decreased with R_o incorporation, indicating the appearance of additional non-radiative recombination pathways from the electronic interaction *via* the heterojunction, further verifying the proposed mechanism of interfacial CT by type-II band alignment. The intensity-average PL lifetime (τ_{av}) was also calculated for better comparison. The τ_{av} of $\text{Na-A}_d/\text{R}_o$ (184.3 ps) is shorter than that of Na-A_d (359.2 ps), indicating outstanding interfacial CT properties which contribute to superior NRR kinetics with an appropriate CB band position. Moreover, photocurrent and electrochemical impedance spectroscopy (EIS) measurements under solar light illumination are ascribed to photoinduced electrons transferring to the electrode (Fig. 4g and S22†).¹⁴ The increase in photocurrent response and the decrease in CT resistance (R_{CT}) for $\text{Na-A}_d/\text{R}_o$ compared to Na-A_d indicated that photogenerated charge carriers are well separated at the heterojunction (Table S7†), consistent with TRPL analysis. We can further explicate the enhanced charge separation in correlation with NRR activity for $\text{Na-A}_d/\text{R}_o$ by BET specific surface area-normalized NH_3 yield compared to Na-A_d (Table 1).

2.5 Proposed mechanistic pathway for N_2 fixation

To identify the time-dependent change of N-related functional groups in the early stages of the photocatalytic NRR, *in situ* diffuse reflectance infrared Fourier transform (*in situ* DRIFT) measurements were conducted (Fig. S23†).^{11,14,45} To exclude the background spectra of adsorbed gas and impurities, the sample was fully dried at 333 K in a vacuum oven overnight, and then



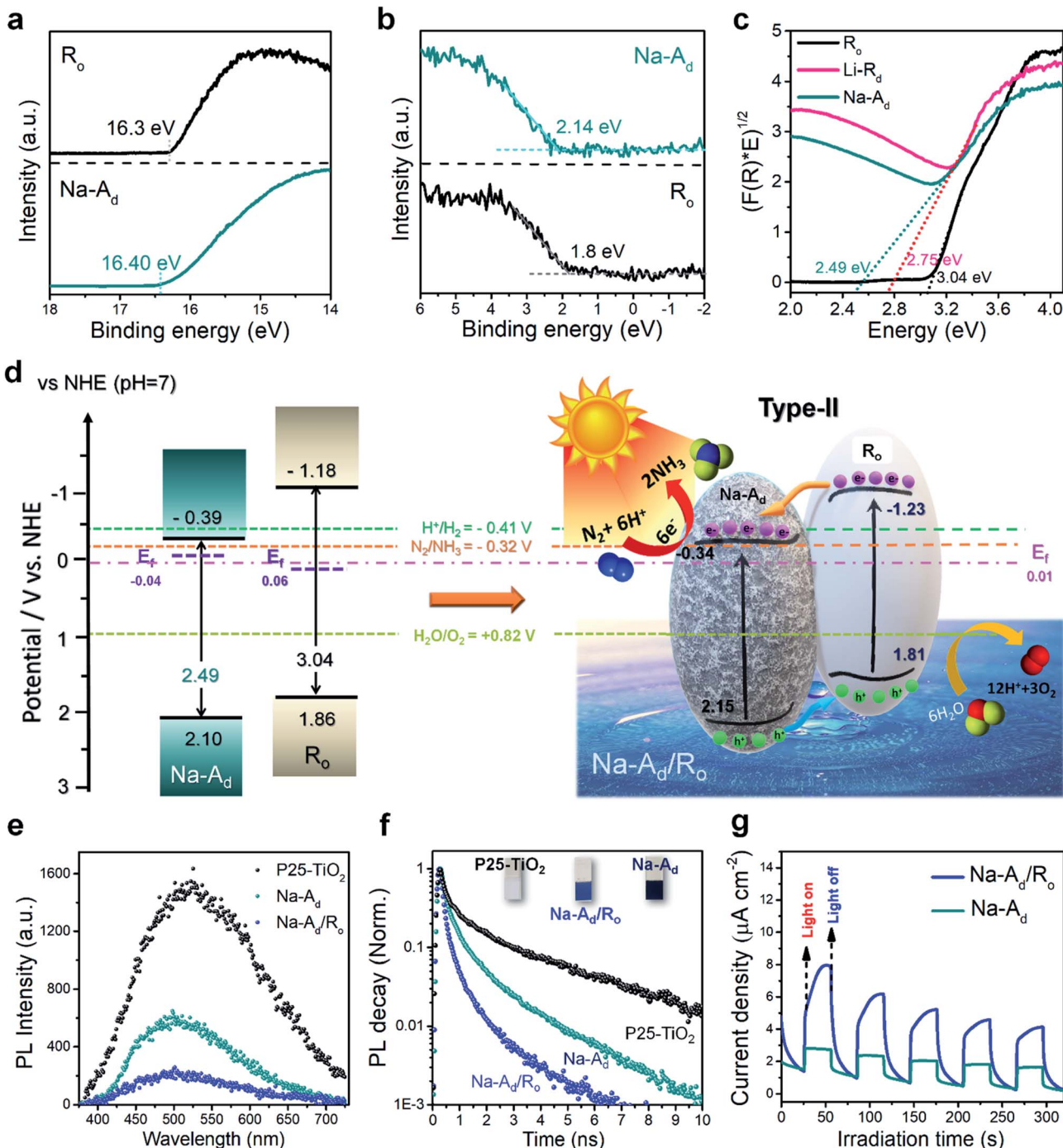


Fig. 4 Spectroscopic analysis for possible charge carrier dynamics and the corresponding energy level diagram depicting the photochemical reaction. (a) UPS spectra and (b) valence band XPS edge spectra of R_o and $Na-A_d$. (c) Kubelka-Munk function versus the photon energy graphs and calculated bandgap of R_o , $Li-R_d$, and $Na-A_d$. (d) Estimation of energy band structures of $Na-A_d$, R_o , and $Na-A_d/R_o$. (e) Photoluminescence (PL) spectra ($\lambda_{ex} = 375$ nm; $\lambda_{em} = 506$ nm) and (f) time-resolved photoluminescence (TRPL) of P25-TiO₂, $Na-A_d$ and $Na-A_d/R_o$. The scatter points were fitted using a biexponential decay. (g) Transient photocurrent response of $Na-A_d/R_o$ and $Na-A_d$.

was placed into a DRIFT specimen chamber. Several absorption bands gradually increase under 1 sun irradiation from 0 to 60 min in the range of 1100–1700 cm^{-1} (Fig. 5a). The FT-IR spectra of N-related functional groups represent six bands: 1123, 1289, 1329, 1425, 1551, and 1660 cm^{-1} . The interference from CO_2 and H_2O from the air was removed by a background

calibration. The bands at 1123 and 1660 cm^{-1} can be assigned to N–N stretching in chemisorbed N_2H_4 species on catalysts. Two weak bands at 1329 and 1551 cm^{-1} are characteristic of adsorbed NH_3 and sharp bands at 1289 and 1425 cm^{-1} can be assigned to adsorbed NH_4^+ ($-\text{NH}_2$ wagging and H–N–H bending of adsorbed N_2H_4 species, respectively), which are intensified

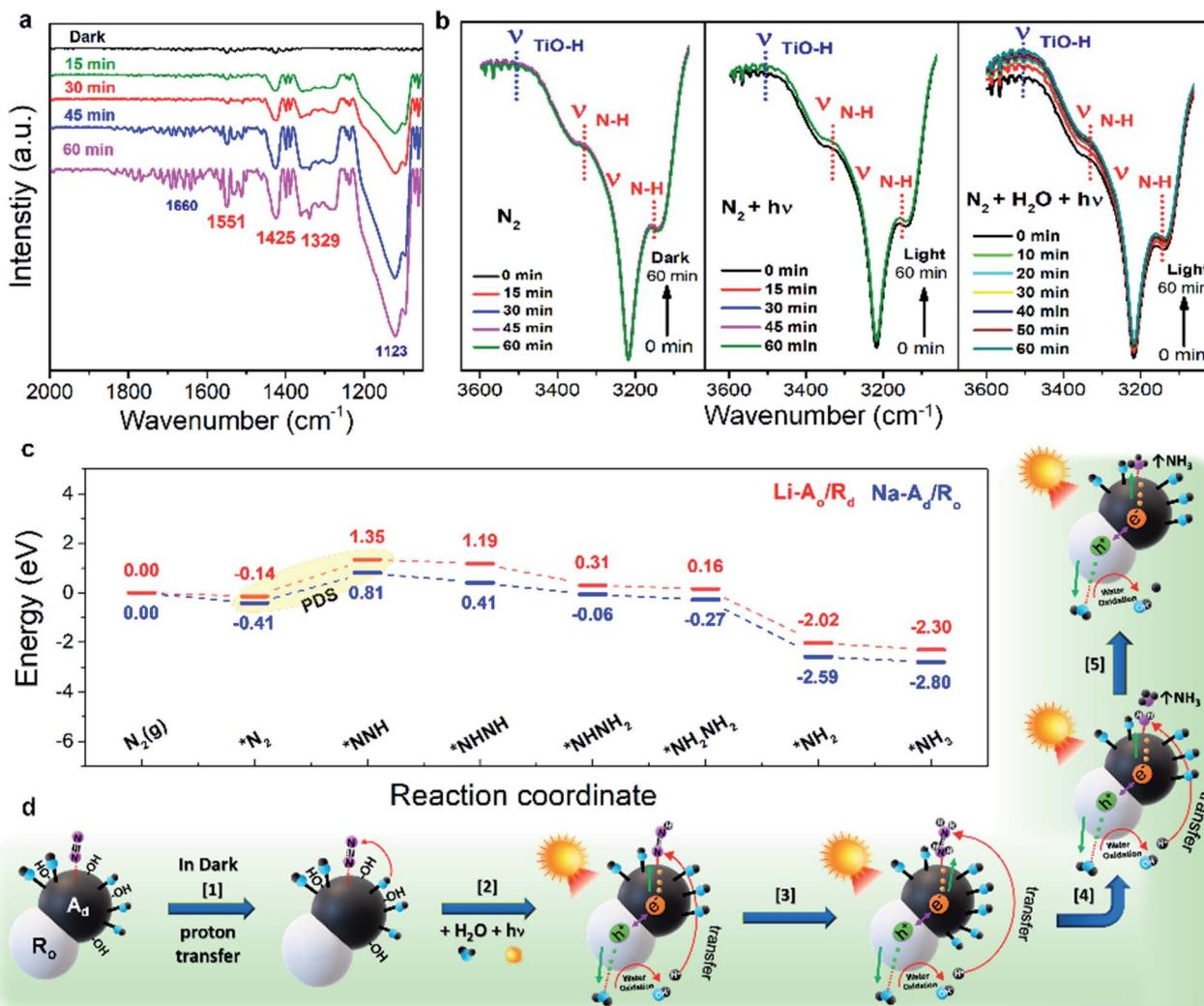


Fig. 5 Proposed mechanistic pathway for N_2 fixation. (a) Fourier Transform Infrared (FT-IR) spectra during the N_2 reduction reaction in the presence of water and N_2 under solar illumination for 60 min. (b) Time-dependent change of *in situ* Diffuse Reflectance Infrared Fourier Transform (DRIFT) spectra of Na-Ad/R_o after N_2 adsorption in the dark for 60 min, sunlight irradiation for 60 min and then water vapor supply for 60 min simultaneously (from left to right) under ambient conditions. (c) Gibbs free energy diagram of the N_2 reduction reaction on Na-Ad/R_o and Li-Ad/R_d . (d) Schematic illustration of the alternating pathway during the photocatalytic N_2 fixation on Na-Ad/R_o .

with the increase of reaction time. Absorption bands in the range of 3100–3600 cm^{-1} for Na-Ad/R_o and Na-Ad_d are shown in Fig. 5b and S24.† The intensity of peaks at 3150 and 3334 cm^{-1} attributed to an N–H stretching mode ($\nu_{\text{N–H}}$) gradually increases, followed by the increased peaks at 3527 cm^{-1} assigned to the O–H stretching ($\nu_{\text{TiO–H}}$) mode after water supply.⁴⁶ As a result, *in situ* measurements elucidate that inert $\text{N}\equiv\text{N}$ is efficiently activated on phase-selective defect sites on Na-Ad/R_o under 1 sun irradiation, leading to the subsequent $\text{N}\equiv\text{N}$ cleavage to NH_3 or NH_4^+ at the last step.

To gain further insight into the NRR mechanism of phase-selective defect sites over $\text{Li-Ad/R}_d(110)$ and $\text{Na-Ad/R}_o(101)$, the DFT calculations were carried out as shown in Fig. 5c. After successful $^*\text{N}_2$ adsorption, the Gibbs free energy for the first hydrogenation step is significant as a potential determining step (PDS). One can see that the PDS ($^*\text{N}_2$ to N-NH^*) on $\text{Na-Ad}/$

$\text{R}_o(101)$ was indeed favored by a lower energy barrier (1.22 eV), in comparison to 1.49 eV for $\text{Li-Ad}_d/\text{R}_d$, indicating that $\text{Na-Ad}_d/\text{R}_o$ possesses better NRR intrinsic activity than $\text{Li-Ad}_d/\text{R}_d$. Note that the alternating pathway is the thermodynamically favorable process compared to the distal pathway after the PDS (Fig. S25†). Subsequent N-NH^* hydrogenation to NH-NH^* requires a low energy barrier for $\text{Na-Ad}_d/\text{R}_o$ compared to $\text{Li-Ad}_d/\text{R}_d$, which is thermodynamically more feasible during the NRR. Corresponding visual images of different steps involved in the DFT calculation for both $\text{Na-Ad}_d/\text{R}_o$ and $\text{Li-Ad}_d/\text{R}_d$ are presented in Fig. S26.† Based on *in situ* DRIFT and theoretical calculations, we deduced a possible NRR pathway on Na-Ad/R_o in Fig. 5d and additionally, and listed the chemical equations (Discussion S1†). The photo-driven NH_3 synthesis proceeds through the activation of N_2 by the supply of multiple exciton transfer using photons as a driving force. At first, there is a proton-coupled

electron transfer step (Step 1) where the N_2 adsorbed on Ti^{3+} species in Na-A_d ($^*\text{N}\equiv\text{N}$) interact with H atoms of the adjacent $\text{Ti}^{3+}\text{-OH}$, resulting in the appearance of an N-H stretching vibration ($\nu_{\text{N-H}}$) band. After 1 sun irradiation and water supply (Step 2), protons (H^+) from the oxidized water *via* photo-generated holes (h^+) at the VB of R_o and electrons (e^-) at the CB of Na-A_d generate the adsorbed chemical species ($^*\text{N}=\text{NH}$) as follows: $^*\text{N}\equiv\text{N} + \text{H}^+ + \text{e}^- \rightarrow ^*\text{N}=\text{NH}$. Consequently, transferring four e^- and H^+ to $^*\text{NH}_2\text{-NH}_2$ (Step 3) on Na-A_d produces free- NH_3 (Step 4), and the remaining $^*\text{NH}_2$ is hydrogenated and regenerates the Ti^{3+} sites after NH_3 desorbed from the catalysts for the next N_2 adsorbates (Step 5). This ideal alternating pathway on $\text{Na-A}_\text{d}/\text{R}_\text{o}$ which involves the one-by-one addition of H atoms and electrons to simultaneously break down the $\text{N}\equiv\text{N}$ bond can efficiently produce NH_3 .⁴⁷

3. Conclusions

In summary, superior NRR activity with high selectivity was achieved by phase-selective defect sites on mixed-phase commercial P25- TiO_2 . Our DFT simulations revealed that defect sites on the disordered Na-A_d phase exhibit higher N_2 adsorption ability and better intrinsic NRR activity than those on the disordered Li-R_d phase. Consistently, the experimental findings confirmed highly selective N_2 affinity on defect sites on Na-A_d over Li-R_d . Moreover, Na-A_d can harvest the visible-range spectrum ascribed to the bandgap reduced by Ti^{3+} sites on oxygen vacancies. Upon integration with the R_o phase, a suitable CB band position for the NRR over the HER and rapid interfacial charge separation at the heterointerface for $\text{Na-A}_\text{d}/\text{R}_\text{o}$ facilitate the desired intermediates ($^*\text{N}=\text{NH}$) *via* subsequent hydrogenation steps along with a thermodynamically favorable process verified by charge dynamics and band structure analysis combined with DFT simulations. As a result, noble-metal free $\text{Na-A}_\text{d}/\text{R}_\text{o}$ achieved a superior NH_3 formation rate of $432 \mu\text{mol g}^{-1} \text{h}^{-1}$, which is ~ 125 times higher than that of bare TiO_2 ($3.4 \mu\text{mol g}^{-1} \text{h}^{-1}$) under simulated AM 1.5G light irradiation at room temperature with a high AQE of 13.6%, suppressing H_2 generation. This finding highlights a promising approach to demonstrate the importance of phase-selective active sites with a suitable band position to develop a novel photocatalyst for future energy-related applications.

Data availability

The data that support the findings of this study are available from the corresponding author upon reasonable request.

Author contributions

J. S., X. L. and A. K. equally contributed to this work. J. S. and Y. H. conceived and designed the experiments. J. S. and Y. H. carried out the synthesis of the materials and photocatalytic NRR. X. L. conducted the DFT calculation. A. K., J. Y. and Y. D. K. supported the data analysis and supported *in situ* measurements. E. L. conducted the PL measurements. H. L. supervised the project. J. S., A. K., and H. L. wrote the paper. All authors

discussed the results and commented on the manuscript. All authors have given approval to the final version of the manuscript.

Conflicts of interest

The authors declare no competing financial interest.

Acknowledgements

This work was supported by the Institute for Basic Science (IBS-R0111-D1) and was partially supported by the Korea Medical Device Development Fund grant funded by the Korea government (the Ministry of Science and ICT, the Ministry of Trade, Industry and Energy, the Ministry of Health & Welfare, the Ministry of Food and Drug Safety) (Project Number: KMDF_PR_20200901_0004) and Scale-up Support Program for Environmental Small-Medium Enterprise (00005002700).

References

- 1 R. F. Service, *Science*, 2014, **345**, 610.
- 2 J. W. Erisman, M. A. Sutton, J. Galloway, Z. Klimont and W. Winiarwter, *Nat. Geosci.*, 2008, **1**, 636.
- 3 C. J. M. van der Ham, M. T. M. Koper and D. G. H. Hetterscheid, *Chem. Soc. Rev.*, 2014, **43**, 5183.
- 4 S. Li, Y. Wang, J. Liang, T. Xu, D. Ma, Q. Liu, T. Li, S. Xu, G. Chen, A. M. Asiri, Y. Luo, Q. Wu and X. Sun, *Mater. Today Phys.*, 2021, **18**, 100396.
- 5 Q. Liu, T. Xu, Y. Luo, Q. Kong, T. Li, S. Lu, A. A. Alshehri, K. A. Alzahrani and X. Sun, *Curr. Opin. Electrochem.*, 2021, **29**, 100766.
- 6 T. Xu, B. Ma, J. Liang, L. Yue, Q. Liu, T. Li, H. Zhao, Y. Luo, S. Lu and X. Sun, *Acta Phys.-Chim. Sin.*, 2021, **37**(7), 2009043.
- 7 T. Wang, S. Li, B. He, X. Zhu, Y. Luo, Q. Liu, T. Li, S. Lu, C. Ye, A. M. Asiri and X. Sun, *Chin. J. Catal.*, 2021, **42**, 1024–1029.
- 8 T. Wang, Q. Liu, T. Li, S. Lu, G. Chen, X. Shi, A. M. Asiri, Y. Luo, D. Ma and X. Sun, *J. Mater. Chem. A*, 2021, **9**, 884–888.
- 9 X. Chen, N. Li, Z. Kong, W.-J. Ong and X. Zhao, *Mater. Horiz.*, 2018, **5**, 9–27.
- 10 Q. Liu, L. Ai and J. Jiang, *J. Mater. Chem. A*, 2018, **6**, 4102–4110.
- 11 Y. Zhao, R. Shi, X. Bian, C. Zhou, Y. Zhao, S. Zhang, F. Wu, G. I. N. Waterhouse, L.-Z. Wu, C.-H. Tung and T. Zhang, *Adv. Mater.*, 2019, **31**, 1806482.
- 12 H. Jia, A. Du, H. Zhang, J. Yang, R. Jiang, J. Wang and C.-Y. Zang, *J. Am. Chem. Soc.*, 2019, **141**, 5083–5086.
- 13 Y. Shiraishi, M. Hashimoto, K. Chishiro, K. Moriyama, S. Tanaka and T. Hirai, *J. Am. Chem. Soc.*, 2020, **142**, 7574–7583.
- 14 P. Li, Z. Zhou, Q. Wang, M. Guo, S. Chen, J. Low, R. Long, W. Liu, P. Ding, Y. Wu and Y. Xiong, *J. Am. Chem. Soc.*, 2020, **142**, 12430–12439.
- 15 C. Gao, J. Low, R. Long, T. Kong, J. Zhu and Y. Xiong, *Chem. Rev.*, 2020, **120**, 12175–12216.
- 16 C. Liu, X. Niu, Q. Li, A. Du and J. Wang, *J. Am. Chem. Soc.*, 2019, **141**, 2884–2888.



17 C. Zhang, D. Wang, Y. Wan, R. Lv, S. Li, B. Li, X. Zou and S. Yang, *Mater. Today*, 2020, **40**, 18–25.

18 H. Hirakawa, M. Hashimoto, Y. Shiraishi and T. Hirai, *J. Am. Chem. Soc.*, 2017, **139**, 10929.

19 K. Zhang, L. Wang, J. K. Kim, M. Ma, G. Veerappan, C.-L. Lee, K.-j. Kong, H. Lee and J. H. Park, *Energy Environ. Sci.*, 2016, **9**, 499–503.

20 H. Hwang, S. Oh, J. Shim, Y. Kim, A. Kim, D. Kim, J. Kim, S. Bak, Y. Cho, V. Q. Bui, T. A. Le and H. Lee, *ACS Appl. Mater. Interfaces*, 2019, **11**, 35693.

21 H. Choi, J. Lee, D. Kim, A. Kumar, B. Jeong, K.-j. Kim, H. Lee and J. Y. Park, *Catal. Sci. Technol.*, 2021, **11**, 1698–1708.

22 J. Lee, A. Kumar, T. Yang, X. Liu, A. R. Jadhav, G. H. Park, Y. Hwang, J. Yu, C. T. K. Nguyen, Y. Liu, S. Ajmal, M. G. Kim and H. Lee, *Energy Environ. Sci.*, 2020, **13**, 5152–5164.

23 S. Z. Andersen, V. Čolić, S. Yang, J. A. Schwalbe, A. C. Nielander, J. M. McEnaney, K. Enemark-Rasmussen, J. G. Baker, A. R. Singh, B. A. Rohr, M. J. Statt, S. J. Blair, S. Mezzavilla, J. Kibsgaard, P. C. K. Vesborg, M. Cargnello, S. F. Bent, T. F. Jaramillo, I. E. L. Stephens, J. K. Nørskov and I. Chorkendorff, *Nature*, 2019, **570**, 504–508.

24 L.-B. Xiong, J.-L. Li, B. Yang and Y. Yu, *Nanomater*, 2012, **2012**, 831524.

25 A. Naldoni, M. Altomare, G. Zoppellaro, N. Liu, Š. Kment, R. Zbořil and P. Schmuki, *ACS Catal.*, 2019, **9**, 345–364.

26 Y. Liu, Q. Xu, X. Fan, X. Quan, Y. Su, S. Chen, H. Yu and Z. Cai, *J. Mater. Chem. A*, 2019, **7**, 26358–26363.

27 P. Kuśtrowski, L. Chmielarz, E. Bożek, M. Sawalha and F. Roessner, *Mater. Res. Bull.*, 2004, **39**, 263–281.

28 G. Kresse and J. Furthmüller, *Comput. Mater. Sci.*, 1996, **6**, 15–50.

29 G. Kresse and J. Furthmüller, *Phys. Rev. B: Condens. Matter Mater. Phys.*, 1996, **54**, 11169–11186.

30 J. P. Perdew, K. Burke and M. Ernzerhof, *Phys. Rev. Lett.*, 1996, **77**, 3865–3868.

31 H. J. Monkhorst and J. D. Park, *Phys. Rev. B: Solid State*, 1976, **13**, 5188–5192.

32 E. Skúlason, T. Bligaard, S. Gudmundsdóttir, F. Studt, J. Rossmeisl, F. Abild-Pedersen, T. Vegge, H. Jónsson and J. K. Nørskov, *Phys. Chem. Chem. Phys.*, 2012, **14**, 1235–1245.

33 A. Kumar, V. Q. Bui, J. Lee, A. R. Jadhav, Y. Hwang, M. G. Kim, Y. Kawazoe and H. Lee, *ACS Energy Lett.*, 2021, **6**, 354–363.

34 H. Hirakawa, M. Hashimoto, Y. Shiraishi and T. Hirai, *ACS Catal.*, 2017, **7**, 3713–3720.

35 L. F. Greenlee, J. N. Renner and S. L. Foster, *ACS Catal.*, 2018, **8**, 7820–7827.

36 S. Wang, X. Hai, X. Ding, K. Chang, Y. Xiang, X. Meng, Z. Yang, H. Chen and J. Ye, *Adv. Mater.*, 2017, **29**, 1701774.

37 C. Guo, J. Ran, A. Vasileff and S. Qiao, *Energy Environ. Sci.*, 2018, **11**, 45.

38 A. Kumar and S. Bhattacharyya, *ACS Appl. Mater. Interfaces*, 2017, **9**, 41906–41915.

39 S. Parvin, A. Kumar, A. Ghosh and S. Bhattacharyya, *Chem. Sci.*, 2020, **11**, 3893–3902.

40 G. W. Watt and J. D. Chrisp, *Anal. Chem.*, 1952, **24**, 2006–2008.

41 S. Kohtani, A. Kawashima and H. Miyabe, *Catalysts*, 2017, **7**(10), 303.

42 Y.-H. Chen, J. K. Ye, Y. J. Chang, T. W. Liu, Y. H. Chuang, W. R. Liu, S. H. Liu and Y. C. Pu, *Appl. Catal., B*, 2021, **284**, 119751.

43 M.-H. Vu, M. Sakar and T.-O. Do, *Catalysts*, 2018, **8**(12), 621.

44 Z. Chen, Y. Hu, J. Wang, Q. Shen, Y. Zhang, C. Ding, Y. Bai, G. Jiang, Z. Li and N. Gaponik, *Chem. Mater.*, 2020, **32**, 1517–1525.

45 H. Yuzawa, T. Mori, H. Itoh and H. Yoshida, *J. Phys. Chem. C*, 2012, **116**, 4126–4136.

46 C. Mao, H. Li, H. Gu, J. Wang, Y. Zou, G. Qi, J. Xu, F. Deng, W. Shen, J. Liu, J. Zhao and L. Zhang, *Chem.*, 2019, **5**, 2702–2717.

47 L. M. Azofra, N. Li, D. R. MacFarlane and C. Sun, *Energy Environ. Sci.*, 2016, **9**, 2545–2549.

